ACS APPLIED MATERIALS & INTERFACES

Research Article

www.acsami.org

Synergistic Effect of Tungsten Carbide and Palladium on Graphene for Promoted Ethanol Electrooxidation

Jun Yang, Ying Xie, Ruihong Wang, Baojiang Jiang, Chungui Tian, Guang Mu, Jie Yin, Bo Wang, and Honggang Fu*

Key Laboratory of Functional Inorganic Material Chemistry, Ministry of Education of the People's Republic of China, Heilongjiang University, Harbin 150080, P. R. China

Supporting Information

ABSTRACT: The synergistic effect of WC and Pd has large benefit for ethanol electrooxidation. The small-sized Pd nanoparticles (NPs) decorated tungsten carbide on graphene (Pd-WC/GN) will be a promising anode catalyst for the direct ethanol fuel cells. The density functional theory (DFT) calculations reveal that the strong interaction exists at the interface between Pd and WC, which induces the electron transfer from WC to Pd. Fortunately, the nanoscale architecture of Pd-WC/GN has been successfully fabricated in our experiments. X-ray photoelectron spectrum further confirms the existence of electron transfer from WC to Pd in a Pd-WC/GN nanohybrid. Notably, electrochemical tests show that the Pd-WC/GN catalyst exhibits low onset potential, a large electrochemical surface area, high activity, and stability for ethanol electrooxidation in alkaline solution compared with Pd/graphene and Pd/commercial Vulcan 72R carbon catalysts. The enhancement can be attributed to the synergistic effect of Pd and WC on graphene. At the interface between Pd and WC, the electron transfer from WC to Pd leads to the increased electron densities of surface Pd, which is available for weakening adsorption of intermediate oxygen-containing species such as CO and activating catalyst. Meanwhile, the increased tungsten oxide induced by electron transfer can facilitate the effective removal of intermediate species adsorbed on the Pd surface through a bifunctional mechanism or hydrogen spillover effect.

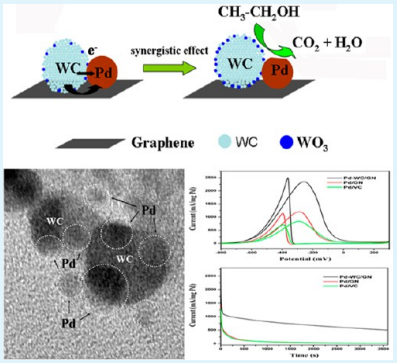

KEYWORDS: *synergistic effect, WC, Pd, graphene, ethanol electrooxidation*

1. INTRODUCTION

Direct alcohol fuel cells have attracted enormous attention as promising power sources for portable electronic devices.[1−3] Among various types of fuel cells, direct methanol and ethanol fuel cells (DMFCs and DEFCs) are promising power sources due to their high energy density, low pollutant emission, low operating temperature, and easy handling. For DEFCs especially, ethanol has low toxicity, high energy density, good stability, easy storage, and low permeability across proton exchange membrane.[4] Importantly, ethanol is a green and renewable resource and can be easily produced from agricultural products or biomass in a large scale.[5,6] Despite these advantages, the low efficiency of ethanol oxidation is insufficient for the further progress and practical application of DEFCs because of the impotent cleavage of C−C bond, inefficient removal of CO, and $-CH_x$ on catalyst active sites.[7,8]

It is generally accepted that Pd-based compositions have enhanced catalytic performance for the formic acid,[9−11] methanol,[12,13] and ethanol electrooxidation.[14,15] Singh[16] have shown that a Pd/graphene electrocatalyst exhibited enhanced performance of ethanol oxidation in alkaline media. To reduce the dosage of noble metal and further improve the catalytic activity, other cheap metals are introduced into Pd metal to form an alloy,[17−20] whereas the stability of these alloyed catalysts is heavily poor because the cheap metals in the alloy are easily dissolved out in the electrolyte during employment. Hence, it is still a formidable challenge as to how to design a low-cost, high-efficient, and stable catalyst for achieving the commercial application of DEFCs.

Tungsten carbide (WC) exhibits also high catalytic activity in fuel cells because of its noble metal-like activity,[21] high stability, and CO poisoning tolerance.[22] Some research has also revealed that WC is able to act as excellent anodic and cathodal materials.[23−27] In our previous study,[28,29] the density functional theory (DFT) calculations indicated the existence of a strong covalent interaction between Pt and WC. Also, many experiments and calculations indicate that WC is utilized as an excellent candidate for fabrication of a high-efficient and stable catalyst system. Therefore, we propose an innovated catalyst system that the small-sized Pd nanoparticles (NPs) are closely deposited on the surface of WC nanocrystals. To detect the interaction between Pd and WC in the Pd-WC nanohybrid, we design in advance a theoretical model of Pd adsorbed on the WC surface. The related calculated results have revealed that when Pd was adsorbed on the WC surface, the total energy of the Pd-WC system was decreased, and the densities of states of

Received: April 3, 2013
Accepted: June 21, 2013
Published: June 21, 2013

   dx.doi.org/10.1021/am401216s | ACS Appl. Mater. Interfaces 2013, 5, 6571−6579

Pd and W at the Pd-WC interface had obvious change, the electron transfer from W to Pd existed in the Pd-WC system. The increased electron densities of the Pd surface are beneficial for weakening adsorption of intermediate oxygen-containing species during the ethanol electrooxidation. The DFT calculations indicated that the fabrication of the Pd-WC system would provide a designed idea to improve catalytic performance in direct ethanol fuel cells. Based on the exciting calculated results, we would be dedicated in the synthesis of the Pd-WC nanohybrid via the advanced material synthesis skill.

It is well-known that graphene can be used as an excellent catalytic support owing to its large surface area, outstanding electronic conductivity, and high electrochemical stability.[30−32] Graphene is utilized as support for depositing a Pd-WC nanohybrid. In our paper, WC nanocrystals are first loaded on graphene (WC/GN) through directly thermal treatment of WO_3-nH_2O/graphene, which is prepared by hydrothermal processing for the acid solution containing graphene oxide and Na_2WO_4 as a green and low-cost tungsten source. The obtained WC/GN acts as a novel support for loading the small-sized Pd NPs through the $NaBH_4$ reducing method (Pd-WC/GN). The results of XPS further indicate that the electron transfer from WC to Pd exists in Pd-WC/GN, which is well consistent with DFT calculations. Notably, the Pd-WC/GN electrocatalyst shows low onset potential, a large electrochemical surface area, excellent activity, and stability for ethanol electrooxidation which can be contributed to the synergistic effect of Pd and WC on graphene. At the interface between Pd and WC on graphene, the electron transfer from WC to Pd has two advantages for ethanol electrooxidation. On the one hand, it can increase the electron densities of the Pd surface and weaken adsorption of intermediate poison-species CO. On the other hand, it leads to the increased tungsten oxide at the interface of Pd-WC which facilitates the effective removal of adsorbed intermediate species through a bifunctional mechanism or hydrogen spillover effect.

2. EXPERIMENTAL SECTION

2.1. Density Functional Calculations. Calculations were performed within the density functional theory (DFT) framework embedded in the CASTEP code. The exchange-correlation energy was treated with the RPBE functional of generalized gradient approximation (GGA) form.[33] The electronic wave functions at each k-point were expanded in terms of a plane-wave basis set, and an energy cutoff of 300 eV was employed. With the application of ultrasoft pseudopotential (USP),[34] the sampling over the Brillouin zone (BZ) was treated by a (8 × 8 × 1) Monkhorst−Pack mesh.[35] The original valence configurations for W, C, and Pd atoms were $5s^25p^65d^4\ 6s^2$, $2s^22p^2$, and $4s^24p^64d^85s^2$, respectively. Moreover, to avoid spurious interactions between the periodic images along the z axis, a vacuum region with a length of 12 Å was used. The stable configurations were obtained by geometry optimization with the BFGS (Broyden-Fletcher-Goldfarb-Shannon) algorithm[36] from the ideal unrelaxed structures. The whole optimization procedure was repeated until the average force on the atoms was less than 0.01 eV $Å^{-1}$ and the energy change less than 1.0×10^{-5} eV/atom.

2.2. The Preparation of WC/GN. The preparation detail of graphene oxide (GO) is seen in the Supporting Information. First, GO powder (200 mg) is dispersed into 200 mL of distilled water, and ultrasonic treatment was carried out for 2 h. Then, Na_2WO_4 (100 mg) is added into the GO solution, and ultrasonic treatment is continued for 30 min to be dissolved completely. Afterward, the solution is adjusted to acidity. The solution was then transferred to a Teflon-lined stainless steel autoclave and hydrothermally treated at 150 °C for 6 h. After cooling down naturally, the black precipitate was separated by centrifugation and thoroughly washed with deionized water and ethanol. The product was vacuum-dried at room temperature (the as-obtained sample is denoted as WO_3-nH_2O/GN). WO_3-nH_2O/GN was loaded into a tube furnace and calcined under high-purity nitrogen (99.99%) protecting at 1100 °C. The as-obtained solid is denoted as WC/GN. As control, graphene nanosheet (GN) is synthesized by the same method.

2.3. The Synthesis of the Pd-WC/GN Electrocatalyst. Pd nanoparticles (NPs) supported on the WC/GN (Pd-WC/GN) catalyst was prepared by the typical $NaBH_4$ reduction method. The as-prepared WC/GN composite (20 mg) was added into 23.5 mL of H_2PdCl_4 solution (2 mM) and ultrasonicated to form the dispersed slurry. The loading of Pd was controlled to be 20 wt %. Excessive $NaBH_4$ solution was added into the mixed solution under vigorously stirring for 2 h at ambient temperature. Then the product was filtered and rinsed thoroughly with distilled water and then vacuum-dried. The final product is denoted as Pd-WC/GN. Similarly, Pd NPs with the same loading content (20 wt %) are supported on GN and commercial Vulcan-72R carbon by the same procedures. The two samples are denoted as Pd/GN and Pd/VC, respectively.

2.4. Characterization. The crystal structure of the sample was characterized using X-ray diffraction equipment (XRD, Cu Kα radiation, λ = 1.5406 Å). The size and morphology of the sample were observed using transmission electron microscope (TEM, JEM-2100, acceleration voltage of 200 kV). The nitrogen adsorption/desorption isotherms were measured by a TriStar II 3020 at 77 K. The surface composition of the samples was characterized by X-ray photoemission spectroscopy (XPS, Kratos-AXIS ULTRA DLD).

2.5. Electrochemical Measurements. Electrochemical measurements were performed using a three-electrode test cell at room temperature. Platinum gauze was used as the counter electrode, and a saturated calomel electrode (SCE) served as the reference electrode. The glassy carbon (GC) electrode (4 mm in diameter) coated with the catalyst was used as the work electrode. The preparation of the work electrode is as follows: 4 mg of the catalyst was dispersed into 2 mL of ethanol by sonication; 8.9 μL of the catalyst suspension was dropped onto the surface of the GC electrode and dried with an infrared lamp; 4.5 μL of Nafion solution (0.5%) was placed on the surface of the GC electrode modified with the above material and dried before electrochemical experiments. The electrolyte for electrochemical measurements was a solution containing 1 M ethanol and 1 M KOH. The solution was deaerated with N_2 before measurements. CO stripping measurement was performed as follows: after purging the solution with N_2 for 20 min, CO was bubbled for 15 min to form a CO adsorbed layer on the catalysts while maintaining the potential at −0.8 V. Excess CO in solution was purged with N_2 for 20 min, and a CO stripping curve was recorded in 1.0 M KOH at 50 mV s^{-1}.

3. RESULTS AND DISCUSSION

In our study, we designed a novel catalyst system of Pd-WC for ethanol electrooxidation. To explore the interaction between Pd and WC, density functional theory (DFT) calculations were performed. The theoretical model of Pd adsorbed on the WC surface was shown in Figure 1. The adsorption energy reflects the bonding strength of an interface and is defined as Equation ($E_{bind} = E_{comp} - E_{Pd} - E_{WC}$), in which E_{comp}, E_{Pd}, and E_{WC} are denoted as the total energies of the Pd-WC hybrid, Pd layers, and WC layers, respectively. The calculated results (in Table S1) showed that the total energy of the Pd-WC system decreases when Pd is adsorbed on the surface of WC, and the calculated adsorption energy of −7.9651 J/m^2 indicated a certain interaction existed in the interface of Pd and WC.

To further clarify the interfacial interaction, the densities of state (DOS) were calculated. In all calculations, the Fermi energy was taken as zero point ($E - E_f = 0$ eV). As shown in Figure 2a, after Pd adsorbed on the WC surface, the DOS of the Pd layer at the interface moves to a lower energy position,

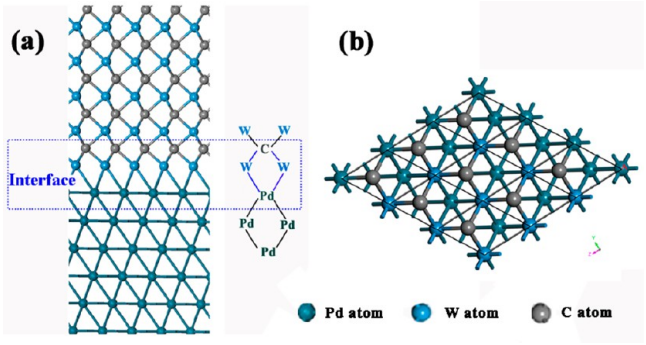

Figure 1. Theoretical model for the Pd-WC heterostructure. (a) Side view, Pd and WC component contains six and ten atomic layers, respectively; (b) Top view for a 3 × 3 supercell.

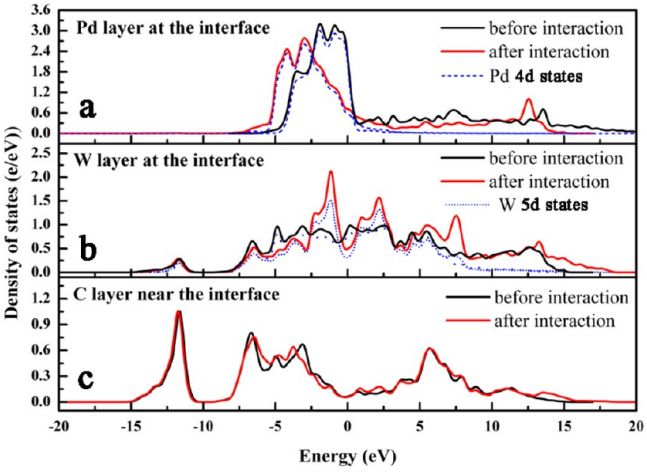

Figure 2. Variations of densities of states (DOS) of (a) the Pd layer, (b) the W layer, and (c) the C layer near the interface caused by Pd adsorption on the WC surface.

and further analysis reveals that the DOS peaks around the [−5.0 eV, 0.0 eV] interval are mainly dominated by the Pd 4d states. Moreover, the DOS of the W layer at the Pd-WC interface (Figure 2b) was also changed significantly. According to the decomposition of DOS, it can be identified that the changed DOS is mainly composed of W 5d states. However, the DOS of the C layer near the interface (Figure 2c) has no obvious change. The results shown in Figure 2a and 2b together confirmed the interactions between Pd 4d and W 5d states at the Pd-WC interface. Due to such an interaction, the charge density at the interface may be changed. The variation of charges can be obtained from the difference between surface and interface atomic charges, which were calculated according to the Mulliken scheme.[37] The calculated layer charges (listed in Table S1) suggest the W layer at the interface lost 0.20e and partially transfers to the Pd layer (−0.11e) at the interface of the Pd-WC system, which well explains the results of Figure 2(a). Therefore, the above calculated results adequately indicate the electron transfer exists in the interface of Pd and WC.

The DFT calculations can provide a promising idea for the fabrication of a high-efficient catalyst for ethanol electro-oxidation. According to the calculated results, we have successfully synthesized the Pd-WC/GN catalyst. Figure 3 shows the TEM images with different magnifications of Pd-WC/GN. As seen in Figure 3a, WC NPs (black dots) have well dispersion on graphene. After magnifying the white region in

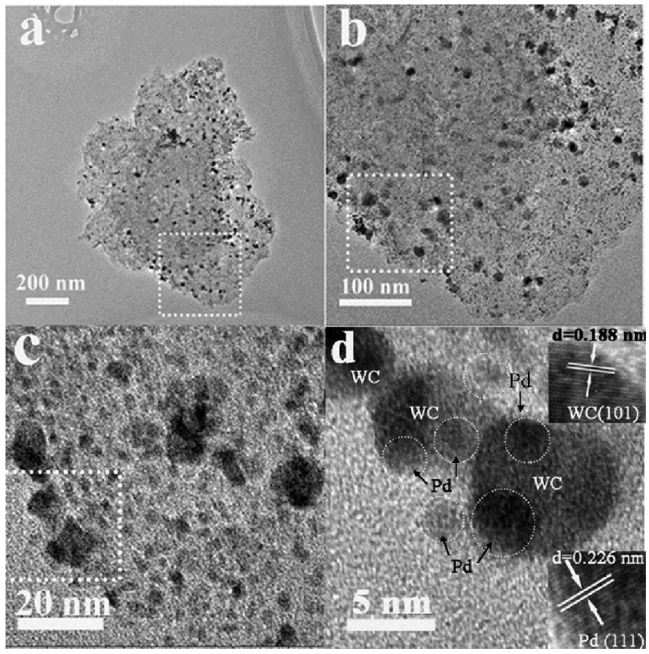

Figure 3. (a, b, c) TEM images with different magnifications and (d) HRTEM of Pd-WC/GN.

Figure 3a, as shown in Figure 3b and 3c, small-sized Pd NPs with ∼3 nm are uniformly and densely dispersed around WC NPs on graphene. Besides, some Pd NPs have also tight growth on the surface of WC NPs. The high resolution TEM image of Pd-WC/GN in Figure 3d shows that small-sized Pd NPs are closely contacted with WC NPs (∼10 nm) on graphene. The inset of Figure 3d displays the well-defined lattice fringes of the WC(101) crystal plane and the (111) crystal plane of Pd NP surrounding WC. The tight contact of Pd NPs with WC NPs is indispensability for achieving the synergetic effect between Pd and WC.

The XRD pattern of WO_3-nH_2O/GN is shown in Figure S1. A series of diffraction peaks in Figure S1 are assigned to WO_3-nH_2O. After heat treatment for WO_3-nH_2O/GN, the diffraction peaks of WC/GN are clearly shown in Figure 4a. The slight diffraction peak at 25.2° is characteristic of C (002) of graphene. The distinct diffraction peaks at 31.5°, 35.7°, 48.3°,

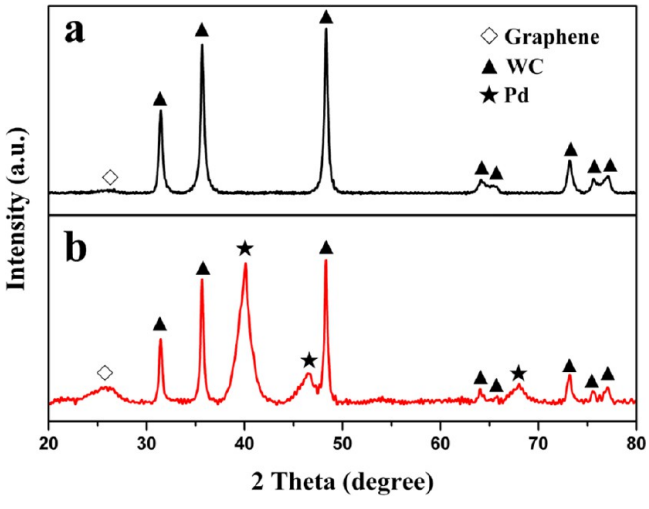

Figure 4. XRD patterns of (a) WC/GN and (b) Pd-WC/GN.

dx.doi.org/10.1021/am401216s | ACS Appl. Mater. Interfaces 2013, 5, 6571−6579

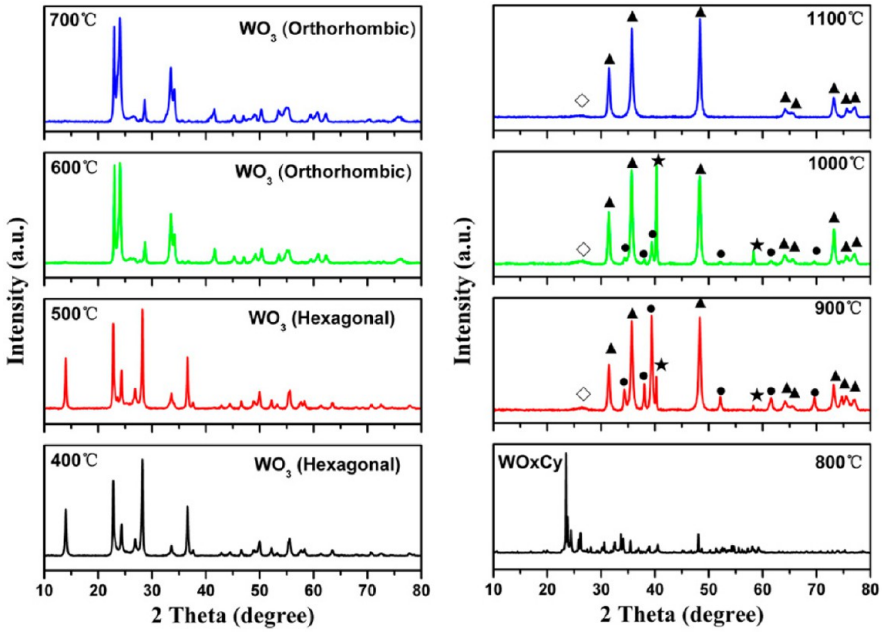

Figure 5. XRD patterns of the samples obtained from the heat treatment for WO_3-nH_2O/GN at different temperature. (Graphene (◊), WC (▲), W_2C (●), W (★)).

64.1°, 65.7°, 73.2°, 75.6°, and 77.1° are indexed as the (001), (100), (101), (110), (002), (111), (200), and (102) planes of the hexagonal WC phase, respectively. This result indicates that the WC/GN nanohybrid is synthesized successfully. On the basis of WC/GN as an efficient catalyst support, small-sized Pd NPs are loaded on WC/GN by the typical $NaBH_4$ reduction method (denoted as Pd-WC/GN). For comparison, graphene and Vulcan-72R carbon are also used as supports for loading Pd NPs with the same content (denoted as Pd/GN and Pd/VC). As shown in the XRD patterns of Pd-WC/GN (Figure 4b) and Pd/GN and Pd/VC (Figure S2), the diffraction peak at 40.1°, 46.5°, and 68.0° are assigned to the (111), (200), and (220) facets of the Pd crystal, respectively.

We synthesized the WC/GN nanohybrid through thermal treatment for the WO_3-nH_2O/GN at 1100 °C under N_2 protecting. In order to clarify the formation mechanism of WC/GN, a series of experiments related with temperature are performed. Figure 5 shows that the XRD patterns of the products obtained from the heat treatment for WO_3-nH_2O/GN at different temperature. For the sake of understanding the phase conversion, the related reactions during the formation of WC/GN are shown in Figure S3. As the temperature is raised to 600 °C, the crystalline phase of WO_3 is transformed from hexagonal into orthorhombic. Continuing to raise the temperature to 800 °C, the partial oxygen of WO_3 is replaced by carbon from graphene, and the tungsten oxycarbide (WO_xC_y) is formed. With the increasing temperature to 900 °C, the oxygen of WO_xC_y is completely replaced by carbon from graphene, and WO_xC_y is transformed to the tungsten carbide (W_nC_m). Meanwhile, W_nC_m is easily decomposed to W_2C, WC, and W under high temperature. Raising the temperature to 1000 °C, W_2C is continually deformed WC and W. At the same time, the W is combined with C from graphene to form WC. When the temperature rises to 1100 °C, the W obtained from the decomposition of W_nC_m is entirely combined with carbon to form WC. It is concluded that tungsten species undergo a series of phase change in the sequence: Hexagonal WO_3→orthorhombic WO_3→WO_xC_y→W_nC_m→W_2C+WC+W→WC+W→WC. This mechanism is similar to the previous report.[38]

Moreover, we characterize the morphology of the samples before and after thermal treatment using transmission electron microscopy (TEM). The TEM images of WO_3-nH_2O/GN (before thermal treatment) in Figure S4a and S4b reveal that WO_3 NPs with the size of about 5 nm is monodispersed on graphene, and graphene is provided with a smooth surface. However, after thermal treatment (1100 °C, N_2-protecting), the WC/GN sample (Figure S4c and S4d) presents large-sized WC NPs (10 nm), and graphene support also becomes crispate which results in the appearance of some pores on its surface. Obviously, the existence of these pores is significant for increasing the specific surface area of the WC/GN sample.

As catalytic support, the sample with large BET specific surface areas plays an important role in providing better mass transport of reactants to the electrocatalyst. Nitrogen adsorption/desorption is used to measure the specific surface area of samples. After thermal treatment for the WO_3-nH_2O/GN (123.8 m^2/g in Figure S5), the WC/GN (Figure S6) exhibits the larger BET specific surface areas (207.6 m^2/g) and a very narrow pore size distribution (pore size about 8 nm), which is derived from the crispate surface of graphene in the WC/GN, but the BET specific surface area of graphene sample (Figure S6 and Table S2) is only 91.4 m^2/g and its pore size distribution is wider. Compared with graphene, the WC/GN exhibits a larger BET specific surface area, which is due to the existence of WC NPs to avoid graphene from congregating. In addition, we also evaluate the BET specific surface area of the Pd-WC/GN and Pd/GN sample. Compared with WC/GN and GN, both Pd-WC/GN and Pd/GN are provided with reduced BET specific surface areas (131.9 m^2/g and 56.2 m^2/g) which may be caused by the more mass contribution of the Pd metal than specific surface areas to samples. Interestingly, the mesoporous structure is still reserved in the Pd-WC/GN (Figure S6b), the same as the WC/GN support, which is significantly beneficial for the mass transport of reactants to it in the electrocatalytic application.

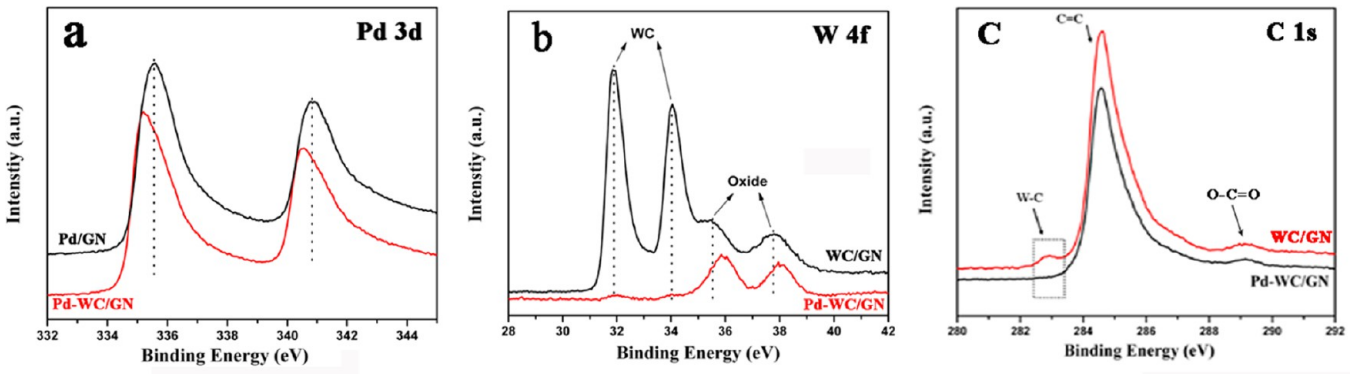

Figure 6. XPS spectra of (a) Pd 3d, (b) W 4f, and (c) C 1s.

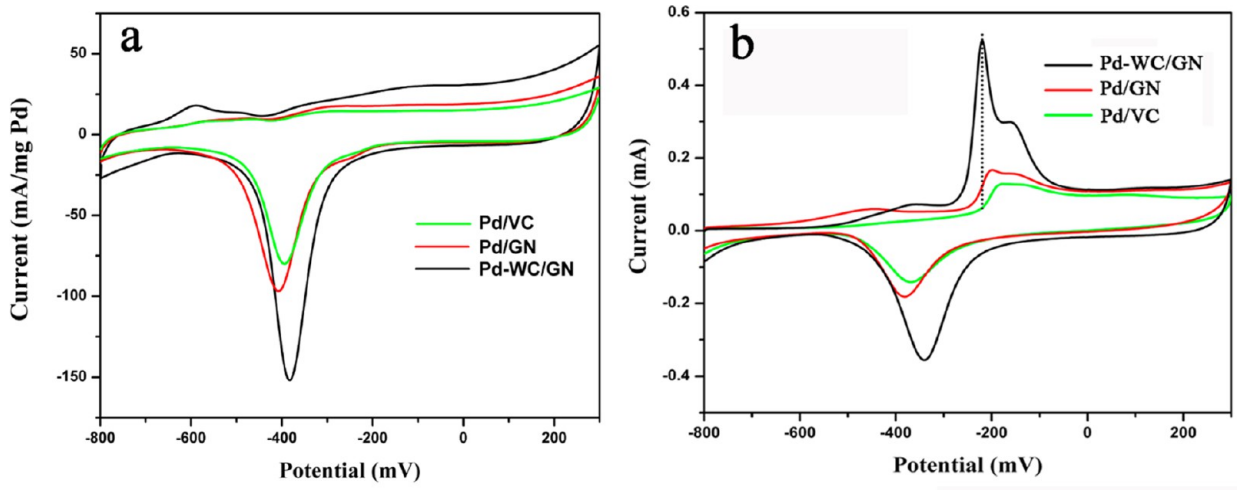

Figure 7. (a) Cyclic voltammograms and (b) CO-stripping curves of different electrodes modified with a catalyst in N_2-protecting 1 M KOH solution at a scan rate of 50 mV s^{-1}.

In order to further testify the interaction between Pd and WC, the surface states of the sample are analyzed by X-ray photoelectron spectrum (XPS). As shown in Figure 6a, the Pd 3d spectrum of Pd/GN shows one doublet with Pd $3d_{5/2}$ binding energy of 335.6 eV and Pd $3d_{3/2}$ binding energy of 340.9 eV, which is characteristic of metallic Pd. Compared with Pd/GN, the Pd 3d spectrum of Pd-WC/GN shows the negative shift of one doublet with Pd $3d_{5/2}$ binding energy (335.2 eV) and Pd $3d_{3/2}$ binding energy (340.5 eV), which is attributed to the electron transfer from WC to Pd metal.[39] This negative shift of Pd 3d binding energy for Pd-WC/GN is similar to the reported literature.[39−41] The DFT calculation results reveal that the electron transfer from W to Pd increases the electron densities of Pd, enhancing the penetration effect of outer-layer electron to the more inner layer. Hence, the increased outer-layer electrons enhance shielding effect for the constraining force of nuclear charge and weaken the attraction of atomic nucleus to 3d electrons. Hence, Pd 3d electrons are more easily inspired and their binding energy would be negative shift. The W 4f spectrum of WC/GN (Figure 6b) shows that the WC phase is predominated on the WC surface, but less tungsten oxide still appears on the WC surface, which arises from the partial oxidation of the WC surface exposed in air. Notably, in contrast to the negative shift of Pd 3d, the W 4f binding energy of Pd-WC/GN shifts positively relative to that of WC/GN, and the tungsten oxide on the WC surface for Pd-WC/GN has also obvious increase in content. This result can be interpreted by the following reason. When Pd NPs are grown on WC/GN, the electron transfer takes place from W d-bond to the Pd metal. Synchronously, W d-bond vacancy results in the positive shift of W 4f binding energy and can be availably combined with oxygen to generate oxide. Moreover, the C 1s spectrum of WC in Pd-WC/GN (the frame in Figure 6c) becomes weak compared with that in WC/GN, indicating that the electron transfer from W to Pd induces the C 1s binding energy of WC to positively shift to 284.6 eV coinciding with the C 1s of graphene support. All in all, the negative shift of Pd 3d binding energy and the positive shift of W 4f binding energy for Pd-WC/GN can testify to the electron interaction existing between Pd and WC, which is completely consistent with the DFT calculations. This strong interaction between metal and support is significant for improving the performance of the electrocatalyst.[41]

Herein, we study the electrocatalytic performance of Pd catalysts for ethanol oxidation in the alkaline solution. To avoid the effect of size and loading content of Pd in the different samples on the electrochemical performance, Pd nanoparticles were controllably deposited on the different supports under the completely same conditions. For the sake of better comparison, we have also done the TEM images of the Pd/GN sample (Figure S7). The TEM images of Pd/GN show that the Pd nanoparticles are about 3 nm (same as the size of Pd in Pd-WC/GN) and monodisperse on graphene. Moreover, the actual loading contents of Pd in the samples are determined

dx.doi.org/10.1021/am401216s | ACS Appl. Mater. Interfaces 2013, 5, 6571−6579

Table 1. Catalytic Performance Characteristics of Different Pd Catalysts for Ethanol Electrooxidation in Alkaline Solution

catalysts	reduction potential of Pd oxide (mV)	ESA[a] (m^2/g)	onset potential (mV)	mass activities (mA/mg Pd)	specific activities (A/m^2 Pd)	residual current (mA/mg Pd)
Pd-WC/GN	−383	65.9	−678	2348.9	35.7	501.9
Pd/GN	−407	48.9	−618	1205.6	24.6	19.2
Pd/VC	−393	36.9	−608	841.9	22.8	21.3

[a]The value of ESA is calculated according to the following formula:[44] ESA = Q_H /0.430*[Pd]. The Q_H (mC) consumed during the reduction of Pd oxides has been estimated by integration of the area under the reduction peak of the CVs shown in Figure 7a. A 0.430 mC cm^{-2} is the electrical charge associated with formation of the Pd oxide monolayer, and [Pd] is the loading of Pd on the working electrode.

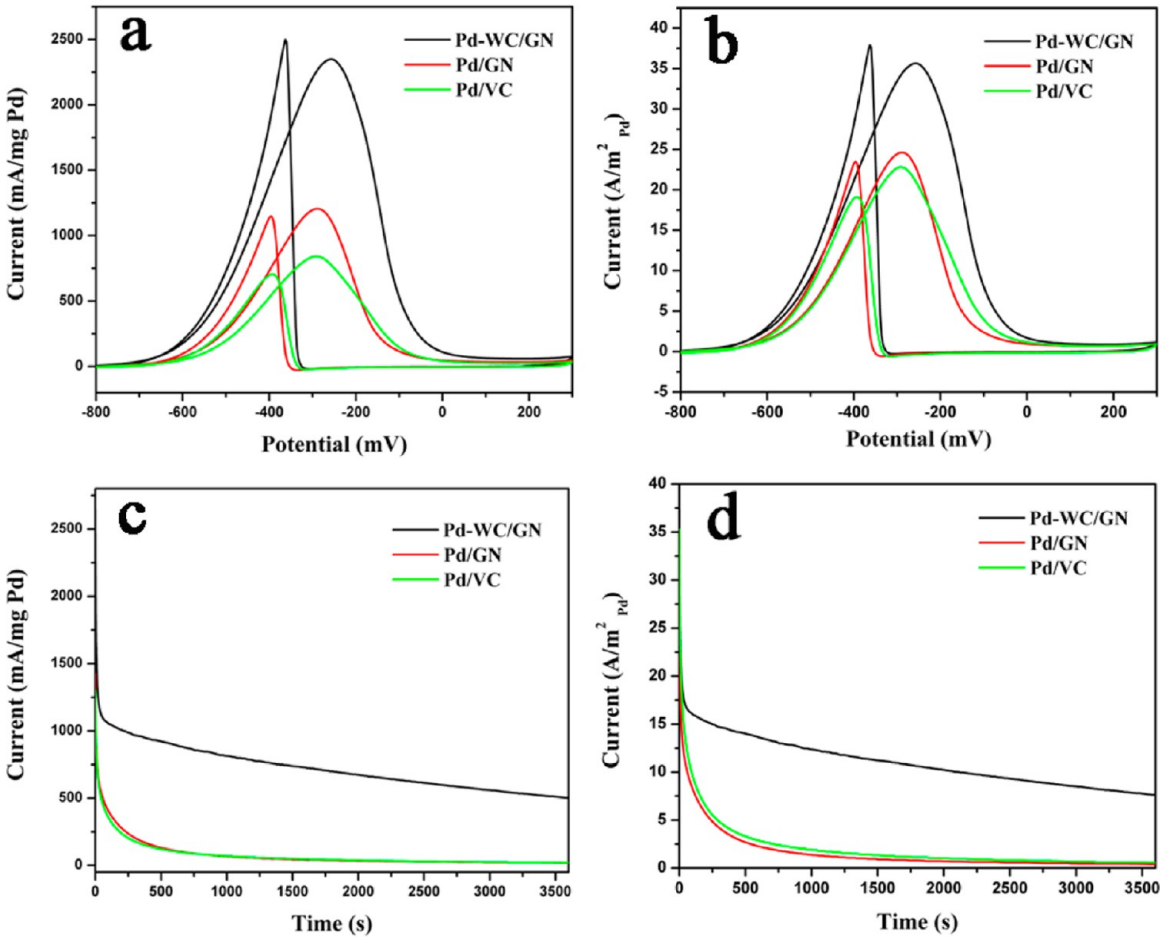

Figure 8. Cyclic voltammograms (a: mass activity; b: specific activity) and current density-time curves (c: mass activity; d: specific activity) of ethanol electro-oxidation on different electrodes in N_2-protecting 1 M ethanol +1 M KOH solution at a scan rate of 50 mV s^{-1}. (Current density is normalized with respect to the mass and ESA of Pd on electrode respectively).

accurately by atomic absorption spectrometry, the measured results also show the Pd actual contents in the catalysts are near theory content of 20 wt %. Therefore, it is reasonable to study the synergistic effect of Pd and WC on electrochemical performance under the same size and loading content of Pd nanoparticles. Herein, the Pd/GN and Pd/VC are used as referenced catalysts. As shown in Figure 7a, cyclic voltammograms (CV) of different electrodes modified with a catalyst are obtained in N_2-protecting 1 M KOH solution at a scan rate of 50 mV s^{-1}. The reduction peak of Pd oxide is observed clearly at about −0.4 V vs SCE in the cathodic scan. It is interesting to note that the reduction peak potential of Pd oxide also shifted positively on the Pd-WC/GN (−383 mV), relative to that on the Pd/GN (−407 mV) and Pd/VC catalysts (−393 mV). The positive shift of the reduction potential of Pd oxide for the Pd-WC/GN implies that the reduced oxophilicity of the Pd surface can weaken chemisorption with oxygen-species, which is benefited from the electron transfer from WC to Pd. This is more profitably for producing fresh active sites on the Pd surface, which can benefit the ethanol oxidation reactions in fuel cells.[42,43] The electrochemical surface area (ESA) of the Pd catalyst on the electrode surface has been estimated using the charge required to strip surface oxide formed during the anodic sweep according to the reported literature.[44] It is obviously seen in Figure 7a that the peak area of reduction of Pd oxide for Pd-WC/GN is larger than that for Pd/GN and Pd/VC. The calculated results (in the Table 1) reveal that Pd-WC/GN (65.9 m^2/g) is provided with a larger ESA than Pd/GN (48.9 m^2/g) and Pd/VC (36.9 m^2/g). The larger ESA of the Pd-WC/GN

dx.doi.org/10.1021/am401216s | ACS Appl. Mater. Interfaces 2013, 5, 6571−6579

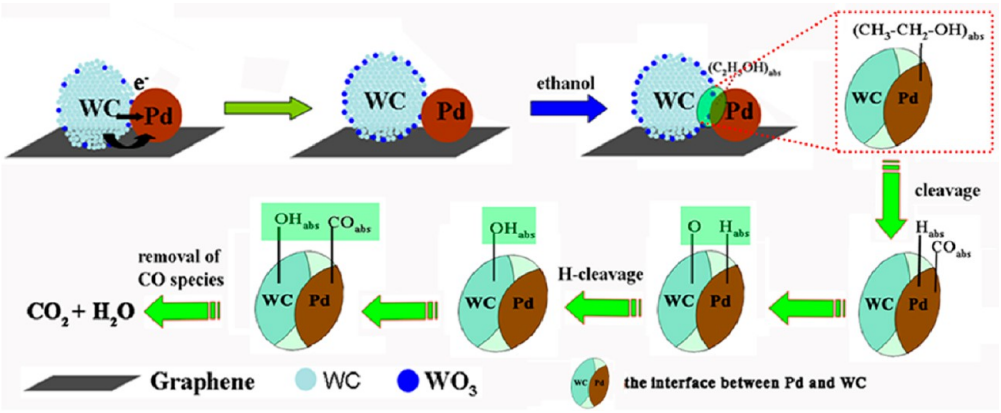

Figure 9. Illustration of the synergetic effect of Pd and WC on graphene for ethanol oxidation.

catalyst is provided with more active sites, which is significant for enhanced electroactivities of the Pd-WC/GN catalyst.

Nørskov and co-workers proposed that there are strong correlations between the d-band center of a metal substrate and the adsorption energy of CO: a downshift of the d-band center leads to a reduction of the adsorption energy.[45,46] The DFT calculation in Figure 2 shows that the 4d-band center of Pd shifted down, which implies the chemical interaction between Pd and CO should be weaker than at pure Pd. Therefore, CO-stripping measurements are significantly available for validating this synergistic effect of Pd and WC in favor of the weakening adsorption of intermediate oxygen-containing species. As seen in Figure 7b, the Pd-WC/GN catalyst exhibits larger peak areas of CO oxidation than Pd/GN and Pd/VC catalysts, which can be originated from the larger ESA of Pd-WC/GN. Meanwhile, the onset potential of CO oxidation on the Pd-WC/GN catalyst (−222 mV) is obviously more negative than that on the Pd/GN (−198 mV) and Pd/VC catalysts (−178 mV). This negative shift indicates that CO molecules are oxidized more easily on the Pd-WC/GN catalyst, implying that the Pd-WC/GN is provided with an improvement in the CO poisoning resistance which can be ascribed to the synergistic effect of Pd and WC.

The CVs of the Pd-based catalysts for ethanol electrooxidation are shown in Figure 8. It is notable in Figure 8a that the onset potential of the Pd-WC/GN catalyst (−678 mV) is smaller than those of the Pd/GN catalyst (−618 mV) and the Pd/VC catalyst (−608 mV), which indicates that the ethanol molecular is easily oxidized on the Pd-WC/GN catalyst. Besides, the Pd-WC/GN catalyst also exhibits a superior mass activity of 2348.9 mA/mg Pd, which is 1.95 times the Pd/GN catalyst (1205.6 mA/mg Pd) and 2.79 times Pd/VC (841.9 mA/mg Pd), respectively. Moreover, to evaluate the effective utilization of the electrochemical surface area of the Pd catalyst, the current density is normalized with respect to the ESA of Pd (shown in Figure 8b). The results in Table 1 indicate that Pd-WC/GN exhibits also a higher specific activity (35.7 A/m^2 Pd) that is 1.45 times Pd/GN (24.6 A/m^2 Pd) and 1.56 times Pd/VC (22.8 A/m^2 Pd), respectively. The excellent activity (mass and specific) of the Pd-WC/GN catalyst could be ascribed to the synergistic effect of Pd and WC on accelerating the oxidation of ethanol molecular.

Furthermore, to evaluate the electrocatalytic activity and stability of the catalysts under continuous operating conditions, long-term chronoamperometric (CA) experiments were carried out in a 1 M KOH + 1 M ethanol solution. Figure 8c demonstrates the CA curves for the Pd-WC/GN, Pd/GN, and Pd/VC electrodes at a constant potential of −0.3 V vs SCE for 3600s. It is noticeable that the Pd-WC/GN after 3600s still retains much higher mass activities of 501.9 mA/mg Pd and is about 26.1 and 23.6 times higher than the Pd/GN (19.2 mA/mg Pd) and Pd/VC (21.3 mA/mg Pd), respectively. Besides, the specific activities (Figure 8d) of the Pd-WC/GN (7.6 A/m^2) is about 19 and 12.7 times higher than the Pd/GN (0.4 A/m^2) and the Pd/VC (0.6 A/m^2). The results indicate the significantly enhanced electrocatalytic activity of Pd-WC/GN under continuous operating conditions. It is well-known that the current decays are associated with the poisoning of the intermediate species on the catalyst. Notably, the Pd-WC/GN has significantly slower current decay compared with the Pd/GN and Pd/VC. This result reveals adequately that the Pd-WC/GN catalyst presents the excellent stability for ethanol oxidation due to the efficient removal of the intermediate species which is derived from the synergetic effect of Pd and WC on graphene.

The forward XPS measurements and DFT calculation results have confirmed a strong interaction between Pd and WC. Furthermore, electrochemical tests have also indicated that this interaction is available to enhance the catalytic performance of the Pd-WC/GN catalyst toward ethanol electrooxidation, which is derived from the cooperated effect of two aspects. (1) Through direct contact pathway or the indirect pathway of graphene, the electron transfer from WC to Pd can not only modify the electronic structure of Pd to enhance the scission of ethanol molecular on Pd active sites, which could be highly related with enhanced electrocatalytic activities,[41,43,47,48] but also increase the electron density of surface Pd which is available for weakening adsorption of intermediate oxygen-containing species such as CO on the Pd surface. (2) Synchronously, as seen in Figure 9, the electron transfer from WC to Pd increases the content of tungsten oxide at the contacted interface between WC and Pd NPs. Hence, the intermediate species adsorbed on Pd sites during the ethanol oxidation can be effectively removed by the adjoined −OH active species on the WC surface via a bifunctional mechanism[49,50] or via a hydrogen spillover effect.[51,52]

4. CONCLUSIONS

On the basis of the DFT calculation of the Pd-WC system, we have successfully synthesized the Pd-WC nanohybrid on graphene (Pd-WC/GN). The XPS results reveal that the electron transfer from WC to Pd occurs obviously in the Pd-

WC/GN and is consistent with the DFT calculation of the Pd-WC system. Compared to Pd/GN and Pd/VC catalysts, the Pd-WC/GN catalyst shows low onset potential, a large electrochemical surface area, high activity, and stability for ethanol electrooxidation in alkaline solution. The excellent performances are benefited from the synergistic effect of Pd NPs and WC. The electron transfer from WC to Pd enables the increase of the electron density of the surface Pd in favor of weakening adsorption of intermediate oxygen-containing species. Also, tungsten oxide on the WC surface derived from electron transfer facilitates the effective removal of intermediate species adsorbed on the Pd surface. Importantly, the enhanced performance of the Pd-WC/GN electrocatalyst for ethanol electrooxidation is promising to promote the commercialization of direct ethanol fuel cells in the future.

■ ASSOCIATED CONTENT

Supporting Information

The preparation of graphene oxide, calculated adsorption energies, and layer charge variations for the Pd-WC system, XRD patterns of WO_3-nH_2O/GN, Pd/GN, and Pd/VC, some reactions during the conversion phase from WO_3/GN to WC/GN, TEM images of WO_3-nH_2O/GN and WC/GN, nitrogen-sorption isotherms and the corresponding pore-size distribution curves of different samples (WO_3-nH_2O/GN, GN, WC/GN, Pd/GN, and Pd-WC/GN), the BET specific surface areas (S_{BET}) of different samples (GN, WC/GN, Pd/GN, and Pd-WC/GN), TEM images of Pd/GN. This material is available free of charge via the Internet at http://pubs.acs.org.

■ AUTHOR INFORMATION

Corresponding Author

*Phone: 86 4518660 9115. Fax: 86 451 8666 1259. E-mail: fuhg@vip.sina.com.

Notes

The authors declare no competing financial interest.

■ ACKNOWLEDGMENTS

We gratefully acknowledge the support of this research by the Key Program Projects of the National Natural Science Foundation of China (No. 21031001), the National Natural Science Foundation of China (No. 20971040, U1034003, 91122018,21101061, 21201058), the Cultivation Fund of the Key Scientific and Technical Innovation Project, Ministry of Education of China (No. 708029), Special Research Fund for the Doctoral Program of Higher Education of China (20112301110002), Natural Science Foundation of Heilongjiang Province (No. B201003).

■ REFERENCES

(1) Jiang, S. P.; Liu, Z. C.; Tian, Z. Q. *Adv. Mater.* **2006**, *18*, 1068−1072.
(2) Antolini, E. *J. Power Sources* **2007**, *170*, 1−12.
(3) Xu, J. B.; Zhao, T. S.; Shen, S. Y.; Li, Y. S. *Int. J. Hydrogen Energy* **2010**, *35*, 6490−6500.
(4) Zhou, W. J.; Song, S. Q.; Li, W. Z.; Zhou, Z. H.; Sun, G. Q.; Xin, Q.; Douvartzides, S.; Tsiakaras, P. *J. Power Sources* **2005**, *140*, 50−58.
(5) Lynd, L. R.; Cruz, C. H. D. B. *Science* **2010**, *330*, 1176.
(6) Lai, S. C. S.; Koper, M. T. M. *Phys. Chem. Chem. Phys.* **2009**, *11*, 10446−10456.
(7) Vigier, F.; Rousseau, S.; Coutanceau, C.; Leger, J. M.; Lamy, C. *Top. Catal.* **2006**, *40*, 111−121.
(8) Huang, M. H.; Li, L. R.; Guo, Y. L. *J. Solid State Electrochem.* **2009**, *13*, 1403−1409.
(9) Yang, J.; Tian, C. G.; Wang, L.; Fu, H. G. *J. Mater. Chem.* **2011**, *21*, 3384−3390.
(10) Yang, J.; Tian, C. G.; Wang, L.; Tan, T. X.; Yin, J.; Wang, B.; Fu, H. G. *ChemPlusChem* **2012**, *77*, 301−307.
(11) Zhao, H.; Yang, J.; Wang, L.; Tian, C. G.; Jiang, B. J.; Fu, H. G. *Chem. Commun.* **2011**, *47*, 2014−2016.
(12) Awasthi, R.; Singh, R. N. *Catal. Sci. Technol.* **2012**, *2*, 2428−2432.
(13) Awasthi, R.; Singh, R. N. *Carbon* **2013**, *51*, 282−289.
(14) Antolini, E. *Energy Environ. Sci.* **2009**, *2*, 915−931.
(15) Bianchini, C.; Shen, P. K. *Chem. Rev.* **2009**, *109*, 4183−4206.
(16) Singh, R. N.; Awasthi, R. *Catal. Sci. Technol.* **2011**, *1*, 778−783.
(17) Ksar, F.; Ramos, L.; Keita, B.; Nadjo, L.; Beaunier, P.; Remita, H. *Chem. Mater.* **2009**, *21*, 3677−3683.
(18) He, Q. G.; Chen, W.; Mukerjee, S.; Chen, S. W.; Laufek, F. *J. Power Sources* **2009**, *187*, 298−304.
(19) Nguyen, S. T.; Tan, D. S. L.; Lee, J. M.; Chan, S. H.; Wang, J. Y.; Wang, X. *Int. J. Hydrogen Energy* **2011**, *36*, 1−8.
(20) Wang, Y.; Nguyen, T. S.; Liu, X. W.; Wang, X. *J. Power Sources* **2010**, *195*, 2619−2622.
(21) Chen, J. G. *Chem. Rev.* **1996**, *96*, 1477−1498.
(22) Levy, R. B.; Boudart, M. *Science* **1973**, *181*, 547.
(23) Weigert, E. C.; Stottlemyer, A. L.; Zellner, M. B.; Chen, J. G. *J. Phys. Chem. C* **2007**, *111*, 14617−14620.
(24) Wang, Y.; Song, S. Q.; Shen, P. K.; Guo, C. X.; Li, C. M. *J. Mater. Chem.* **2009**, *19*, 6149−6153.
(25) Raman, G.; Ham, D. J.; Lee, J. S. *Electrochem. Commun.* **2007**, *9*, 2576−2579.
(26) Liang, C. H.; Ding, L.; Li, C.; Pang, M.; Su, D. S.; Li, W. Z.; Wang, Y. M. *Energy Environ. Sci.* **2010**, *3*, 1121−1127.
(27) Liu, Y.; Mustain, W. E. *ACS Catal.* **2011**, *1*, 212−220.
(28) Wang, R. H.; Xie, Y.; Shi, K. Y.; Wang, J. Q.; Tian, C. G.; Shen, P. K.; Fu, H. G. *Chem.—Eur. J.* **2012**, *18*, 7443−7451.
(29) Wang, R. H.; Tian, C. G.; Wang, L.; Wang, B. L.; Zhang, H. B.; Fu, H. G. *Chem. Commun.* **2009**, *45*, 3104−3106.
(30) Chen, D.; Tang, L. H.; Li, J. H. *Chem. Soc. Rev.* **2010**, *39*, 3157−3180.
(31) Pumera, M. *Chem. Soc. Rev.* **2010**, *39*, 4146−4157.
(32) Wang, L.; Tian, C. G.; Wang, H.; Ma, Y. G.; Wang, B. L.; Fu, H. G. *J. Phys. Chem. C* **2010**, *114*, 8727−8733.
(33) Hammer, B.; Hansen, L. B.; Nørskov, J. K. *Phys. Rev. B* **1999**, *59*, 7413−7421.
(34) Vanderbilt, D. *Phys. Rev. B* **1990**, *41*, 7892−7895.
(35) Monkhorst, H. J.; Pack, J. D. *Phys. Rev. B* **1976**, *13*, 5188−5192.
(36) Pfrommer, B. G.; Cote, M.; Louie, S. G.; Cohen, M. L. *J. Comput. Phys.* **1997**, *131*, 133−140.
(37) Mulliken, R. S. J. *Chem. Phys.* **1955**, *23*, 1833−1846.
(38) Ma, C. A.; Brandon, N.; Li, G. H. *J. Phys. Chem. C* **2007**, *111*, 9504−9508.
(39) Ham, D. J.; Pak, C.; Bae, G. H.; Han, S.; Kwon, K.; Jin, S. A.; Chang, H.; Choi, S. H.; Lee, J. S. *Chem. Commun.* **2011**, *47*, 5792−5794.
(40) Du, C. Y.; Chen, M.; Wang, W. G.; Yin, G. P. *ACS Appl. Mater. Interfaces* **2011**, *3*, 105−109.
(41) Feng, L. G.; Sun, X. J.; Liu, C. P.; Xing, W. *Chem. Commun.* **2012**, *48*, 419−421.
(42) Wang, S.; Jiang, S. P.; White, T. J.; Guo, J.; Wang, X. *J. Phys. Chem. C* **2009**, *113*, 18935−18945.
(43) Guo, S. J.; Dong, S. J.; Wang, E. K. *Energy Environ. Sci.* **2010**, *3*, 1307−1310.
(44) Xiao, L.; Zhuang, L.; Liu, Y.; Lu, J. T.; Abruna, H. D. *J. Am. Chem. Soc.* **2009**, *131*, 602−608.
(45) Hammer, B.; Morikawa, Y.; Nørskov, J. K. *Phys. Rev. Lett.* **1996**, *76*, 2141−2144.
(46) Ruban, A.; Hammer, B.; Stoltze, P.; Skriver, H. L.; Nørskov, J. K. *J. Mol. Catal. A: Chem.* **1997**, *115*, 421.

(47) Park, K. W.; Choi, J. H.; Kwon, B. K.; Lee, S. A.; Sung, Y. E. *J. Phys. Chem. B* **2002**, *106*, 1869−1877.
(48) Zeng, J. H.; Yang, J.; Lee, J. Y.; Zhou, W. J. *J. Phys. Chem. B* **2006**, *110*, 24606−24611.
(49) Micoud, F.; Maillard, F.; Bonnefont, A.; Job, N.; Chatenet, M. *Phys. Chem. Chem. Phys.* **2010**, *12*, 1182−1193.
(50) Kowal, A.; Li, M.; Shao, M.; Sasaki, K.; Vukmirovic, M. B.; Zhang, J.; Marinkovic, N. S.; Liu, P.; Frenkel, A. I.; Adzic, R. R. *Nat. Mater.* **2009**, *8*, 325−330.
(51) Feng, L. G.; Cui, Z. M.; Yan, L.; Xing, W.; Liu, C. P. *Electrochim. Acta* **2011**, *56*, 2051−2056.
(52) McLeod, E. J.; Birssl, V. I. *Electrochim. Acta* **2006**, *51*, 684−693.